International Journal of Aeronautical and Space Sciences (2024) 25:1017–1033
https://doi.org/10.1007/s42405-024-00721-9

IJASS International Journal of Aeronautical and Space Sciences

ORIGINAL PAPER

Research on Integrated Control Method of Coaxial High-Speed Helicopter/Engine Based on Power Prediction Feedforward

Jie Song[1] · Yong Wang[1] · Haoran Guo[1] · Haibo Zhang[1]

Received: 7 August 2023 / Revised: 9 January 2024 / Accepted: 14 February 2024 / Published online: 4 April 2024

Abstract
To effectively meet the high-quality engine control requirements of coaxial high-speed helicopters with variable rotor speed, a novel integrated control method based on power prediction feedforward is proposed. Firstly, an integrated simulation platform of high-speed helicopter/engine is established to reveal the maneuvering characteristics of coaxial high-speed helicopter and the dynamic response of the variable-speed turboshaft engine under various flight conditions. It consists of a simplified coaxial high-speed helicopter model and a variable-speed turboshaft engine. Secondly, an optimal selection method based on random forest is employed to determine the optimal input variables for the demanded power prediction model, which is established through a mini-batch gradient descent neural network. Then, a high-order filter for gas turbine acceleration is designed to further suppress high-frequency interference without losing the low-frequency characteristics of gas turbine acceleration. Finally, the integrated control method based on double feedforward of demanded power prediction is proposed and validated through digital simulation under various typical flight conditions. The results demonstrate that the integrated control method based on double feedforward of demanded power prediction decreases the overshoot and sag of power turbine speed by more than 17.5% and 25.3% in multiple modes, which significantly enhances the dynamic quality of engine control system and enables the swift output of integrated coaxial high-speed helicopter/turboshaft engine system.

Keywords Coaxial high-speed helicopter · Turboshaft engine · Demanded power prediction model · Integrated control method · Fast response control

List of Symbols

H	Flight altitude (m)
$\mathrm{HPA_r}$	Real helicopter demanded power (kW)
$\mathrm{HPA_p}$	Predicted helicopter demanded power (kW)
N_g	Gas turbine speed (%)
N_gdot	Acceleration of gas turbine speed ($1/s^2$)
N_p	Power turbine speed (%)
T_qe	Engine output torque (kN m)
$T_\mathrm{qe,p}$	Predicted engine output torque (kN m)
Vx	Forward speed (m/s)
θ_0	Rotor collective pitch (°)
$\theta_{1\mathrm{s}}$	Longitudinal cycle pitch (°)
θ_P	Pusher propeller pitch (°)
Ω_MR	Coaxial main rotor speed (%)

✉ Haibo Zhang
zh_zhhb@126.com

[1] College of Energy and Power Engineering, Nanjing University of Aeronautics and Astronautics, Nanjing, China

1 Introduction

To overcome the maximum flight speed limitations of helicopters, researchers have devoted to the development of high-speed helicopters since the 1930s [1, 2]. Over the years, coaxial high-speed helicopters such as X2, S-97, and SB-1 have emerged as viable alternatives that are poised to serve as the next generation of military helicopters, owing to their revolutionary coaxial main rotor and pusher propeller layout. This innovative design allows high-speed helicopters to increase the forward flight speed to more than 450 km/h and the range to 1200 km while maintaining the near-ground maneuverability of conventional helicopters [3–5].

One of the primary reasons for such significant improvements in the flight speed of high-speed helicopters is the application of variable rotor speed technology. In contrast to constant main rotor speed, this technology reduces the helicopter flight drag, and ameliorates the helicopter's operational performance and maneuverability by reducing the main rotor speed at high speed, thus avoiding the dynamic

stall of the backward rotor blades and the compression effect at the tip of the forward rotor blades [6]. In addition, the integrated control technology is adopted to achieve coordinated control of the main rotor, transmission system and turboshaft engine, so as to ensure safety and stability during the transition process while increasing the helicopter flight speed [7, 8].

In current practical engineering applications, the turboshaft engines typically adopt the cascade PID control loop to control the gas turbine speed through the inner loop to make the engine respond quickly to the external changes. While the outer loop controls the power turbine speed to maintain the constant speed under all operating conditions. Additionally, the fuel flow is compensated by collective pitch to follow changes in external load and ensure constant engine speed operation [9]. During high-speed flight, the rotor of high-speed helicopter is progressively unloaded while the wing is loaded, and the flight thrust is provided by the pusher propeller at the tail. The collective pitch of the main rotor can no longer fully characterize the demanded power of coaxial high-speed helicopters. Therefore, the engine control system must select more appropriate variables to exactly reflect the demanded power of high-speed helicopters, which helps to meet the requirements for high quality control of variable rotor speed.

Ebert predicted the helicopter demanded power through the lateral cycle pitch variation in yaw maneuvers flight to minimize the overshoot and sag of power turbine speed [10]. In 2002, Smith proposed a torque feedforward control method based on neural network for the engine control system requirements of the Black Hawk helicopter, which enhanced the dynamic response quality of the engine control system [11]. Moreover, Driscoll predicted the demanded torque of helicopter main rotor and tail rotor through polynomial neural network, which further promoted the development of helicopter/engine integrated control technology [12]. Sun designed the incremental cascade controller for turboshaft engine based on auto disturbance rejection control technology, adopting cascade control structure and compensating the controlled object in real-time by expanding state observation to improve the engine power tracking characteristics [13]. According to the cascade control of turboshaft engine based on N_{gdot}, Wang proposed a feedforward compensation method based on the error between the expected output torque and the real output torque of the engine by establishing a rotor torque prediction model [14]. The simulation results show that the overshoot of the power turbine speed can be decreased by 14% compared with the conventional collective pitch feedforward control method.

However, some of the above researches only consider the compensation effect for a specific state of the helicopter, while others only select the collective pitch or torque prediction to characterize demanded power. The demanded power of the twin-rotor and pusher propeller, coaxial main rotor speed and collective pitch, and collective pitch and rotor demanded power all change in reverse during the variable-speed process [15, 16]. It makes the collective pitch inadequate to characterize the demanded power of coaxial high-speed helicopters. Additionally, conventional helicopters adopt constant turbine speed control, thus the engine output torque is consistent with the demanded power change. However, for coaxial high-speed helicopters, the turboshaft engine power turbine speed is no longer constant by changing power turbine speed to change coaxial main rotor speed, hence the change of the demanded power is not completely consistent with the engine output torque. In addition, torque measurement at the rotor has a significant lag relative to the load change, and the response of the engine is insufficient.

Therefore, to make up for the deficiencies of previous research on the integration control methods for coaxial high-speed helicopter/turboshaft engine system, an integrated control method based on power prediction feedforward is proposed. Firstly, an integrated simulation platform of high-speed helicopter/engine is established based on blade-element theory and momentum theory. Secondly, according to the model simulation data, the optimal input set of the demanded power prediction model is determined the optimal selection method of the input characteristic parameters based on the random forest. The demanded power prediction model is then established by MBGD neural network. Thirdly, a double feedforward control structure combined with gain self-adjustment is adopted and an integrated control method based on demanded power prediction is proposed. Then, a high-order filter for gas turbine acceleration is designed to further suppress high-frequency interference of gas turbine acceleration. Finally, the integrated control method based on power prediction feedforward is verified under multiple typical flight conditions and compared with the effect of torque error feedforward control method.

2 Integrated Simulation Platform of High-Speed Helicopter/Engine

To carry out research on the integrated control method of coaxial high-speed helicopter/engine, it is first necessary to establish an integrated simulation platform of high-speed helicopter/engine, which simulates the strong coupling characteristics and dynamic response of real high-speed helicopter/engine. The whole model consists of a simplified model of coaxial high-speed helicopter and a variable-speed turboshaft engine model.

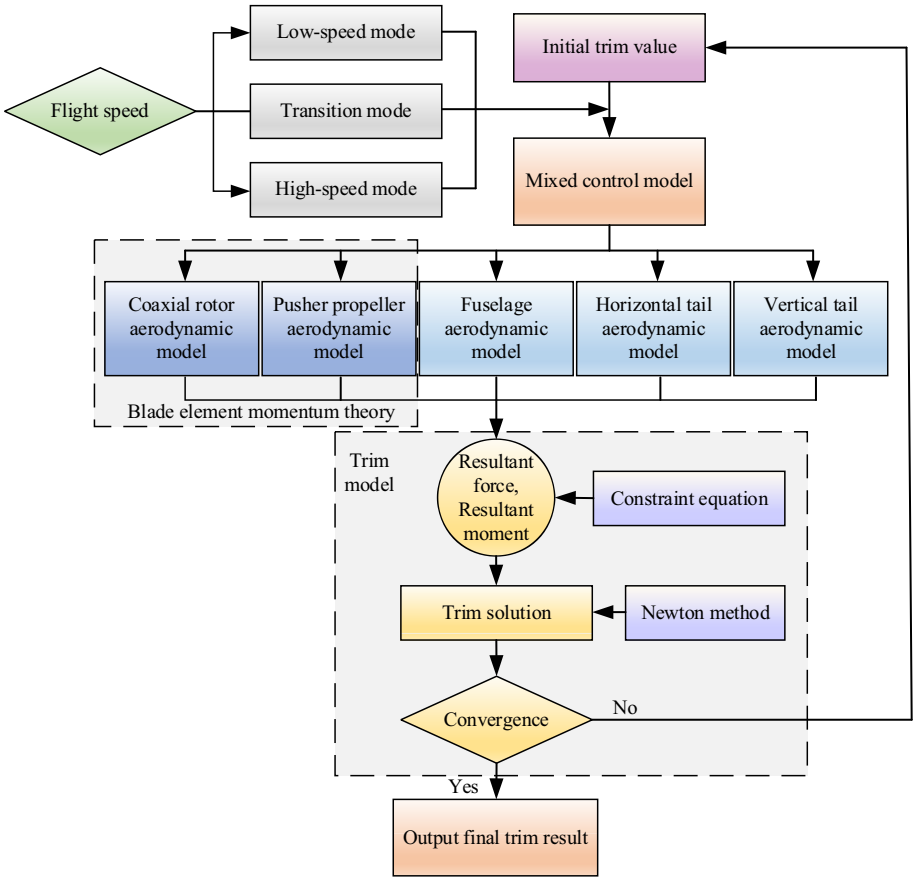

Fig. 1 Flowchart of CHH modeling

2.1 Simplified Coaxial High-Speed Helicopter Model

The coaxial high-speed helicopter is a coaxial compound high-speed helicopter (CHH) with two rigid coaxial main rotors and one pusher propeller. The mathematical model of CHH consists of several subsystems: upper and lower rotors, pusher propeller, fuselage, horizontal tail, and vertical tail. The main modeling process is shown in Fig. 1.

2.1.1 Coaxial Rotor Aerodynamic Model

Owing to the distinctive features of the CHH, there is significant aerodynamic interference between the upper and lower rotors. It is necessary to correct the incidence model by introducing an empirical factor between the upper and lower rotors. The factor as an empirical factor is correlated with the rotor spacing and flight status [17].

The inflow model of the coaxial rotor can be simplified as [18]:

$$\mathbf{M}\begin{pmatrix}\dot{\lambda}_0\\ \dot{\lambda}_C\end{pmatrix}+\mathbf{V}\mathbf{L}^{-1}\begin{pmatrix}\lambda_0\\ \lambda_C\end{pmatrix}=\begin{pmatrix}C_T\\ C_{Mz}\end{pmatrix}, \tag{1}$$

where $\boldsymbol{M}$ denotes the effect of air inertia, $\boldsymbol{V}$ is the mass flow parameter matrix, $\boldsymbol{L}$ embodies the static relationship between the perturbation induced velocity and the perturbation aerodynamic load, C_T is the lift coefficient of the rotor, C_{Mz} is the coefficient of the rotor pitch moment, and λ_0 and λ_C are the dimensionless quantization of the induced velocity, respectively.

Figure 2 illustrates a schematic diagram of the interference of the upper rotor wake on the lower rotor. The wake slipstream of the upper rotor on the paddle disk of the lower rotor causes an interference of the area of S'_L on the lower rotor. The induced velocity of the lower rotor in the area is composed of the induced velocity v_L of the lower rotor and the interference velocity v'_U of the upper rotor on the lower rotor.

According to eddy current theory, the axial induced velocity at distance d below the rotor blade can be approximated in Eq. (2):

$$v_{id}=v_{i0}\left(1+\frac{d}{\sqrt{(R\cos\chi)^2+d^2}}\right)=\varepsilon(d,\chi)v_{i0}, \tag{2}$$

where, v_{i0} is the induced velocity at the paddle disk, R is the rotor radius, and χ is the wake inclination angle.

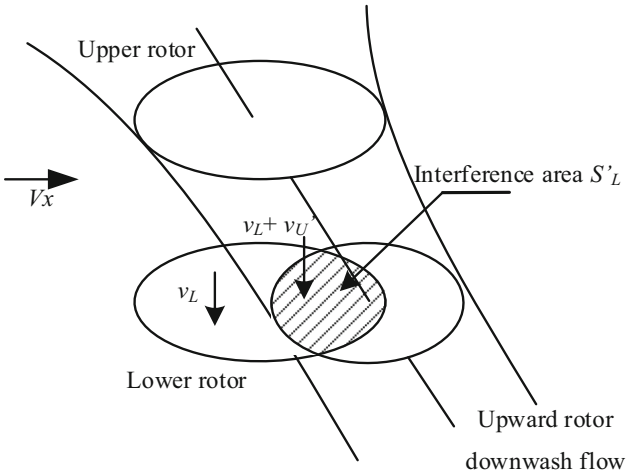

Fig. 2 Interference of upper rotor on lower rotor

By iteratively solving, parameters such as interference area and interference velocity of the upper and lower rotors are obtained. Substitute Eq. (3) to obtain the interference factor δ_{L} of the upper rotor and the interference factor δ_{U} of the lower rotor.

$$\begin{cases} \delta_{\mathrm{L}} = \dfrac{S'_{\mathrm{L}}}{S}\varepsilon(d,\ \chi_{\mathrm{U}}) \\ \delta_{\mathrm{U}} = \dfrac{S'_{\mathrm{U}}}{S}\varepsilon(-d,\ \chi_{\mathrm{L}}) \end{cases}. \tag{3}$$

Consequently, after the introduction of the interference factor, the induced velocities v_{iL} and v_{iU} of the upper and lower rotors are depicted in Eq. (4).

$$\begin{cases} v_{\mathrm{iL}} = v_{\mathrm{L}} + \delta_{\mathrm{L}} v_{\mathrm{U}} + (K_1 v_{\mathrm{CL}} + K_2 \delta_{\mathrm{L}} v_{\mathrm{CU}})\dfrac{r}{R}\cos\psi_{\mathrm{L}} \\ v_{\mathrm{iU}} = v_{\mathrm{U}} + \delta_{\mathrm{U}} v_{\mathrm{L}} + (K_1 v_{\mathrm{CU}} + K_2 \delta_{\mathrm{U}} v_{\mathrm{CL}})\dfrac{r}{R}\cos\psi_{\mathrm{U}} \end{cases}, \tag{4}$$

where v_{L}, v_{U}, v_{CU}, and v_{CL} are calculated from the simplified inflow model. ψ_{L} and ψ_{U} represent the lower and upper rotor azimuth angles, r is the distance of the blade element profile from the flapping hinge, R is the rotor radius, K_1 and K_2 denote the empirical functions of the coaxial rotor wake high angle.

The aerodynamic model of the rotor blade surface is shown in Fig. 3. The lift dL and drag dD calculations of the blade profile are illustrated in Eq. (5).

$$\begin{cases} \mathrm{d}L = \dfrac{1}{2}\rho(\Omega R)^2 a_\infty \alpha b \mathrm{d}r \\ \mathrm{d}D = \dfrac{1}{2}\rho(\Omega R)^2 C_{\mathrm{d}} b \mathrm{d}r \end{cases}, \tag{5}$$

where ρ is the local atmospheric density, a_∞ is the slope of the paddle lift line, α is the angle of attack, b is the profile chord length, and C_{d} is the profile drag coefficient.

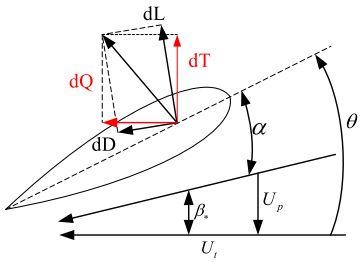

Fig. 3 Aerodynamic model of rotor blade surface

Based on the small-angle assumption, the aerodynamic load on the upper rotor in the hub coordinate is calculated by the blade element theory.

$$\begin{cases} T = \dfrac{k}{2\pi}\displaystyle\int_0^{2\pi}\int_0^{R-l_{hj}} \left(\frac{\mathrm{d}L}{\mathrm{d}r} - \frac{\mathrm{d}D}{\mathrm{d}r}\beta_*\right)\mathrm{d}r\mathrm{d}\psi \\ S = \dfrac{k}{2\pi}\displaystyle\int_0^{2\pi}\int_0^{R-l_{hj}} -\cos\psi\left(\frac{\mathrm{d}L}{\mathrm{d}r}\beta_* + \frac{\mathrm{d}D}{\mathrm{d}r}\right)\mathrm{d}r\mathrm{d}\psi \\ H = \dfrac{k}{2\pi}\displaystyle\int_0^{2\pi}\int_0^{R-l_{hj}} \sin\psi\left(\frac{\mathrm{d}L}{\mathrm{d}r}\beta_* + \frac{\mathrm{d}D}{\mathrm{d}r}\right)\mathrm{d}r\mathrm{d}\psi \\ M_{\mathrm{K}} = \dfrac{k}{2\pi}\displaystyle\int_0^{2\pi}\int_0^{R-l_{hj}} (l_{hj}+r)\left(\frac{\mathrm{d}L}{\mathrm{d}r}\beta_* + \frac{\mathrm{d}D}{\mathrm{d}r}\right)\mathrm{d}r\mathrm{d}\psi \end{cases}, \tag{6}$$

where T is the rotor thrust, S is the lateral force, H is the backward force, M_{K} is the counter-torque, k is the number of blades, l_{hj} is the flapping hinge extension, $\beta*$ is the inflow angle of the profile, and ψ is the blade azimuth angle. Finally, the forces and moments of the upper rotor in the body axis coordinate system are obtained through coordinate transformations.

The aerodynamic model of the lower rotor is similar to that of the upper rotor, but the direction of rotation is opposite, and the counter-torque and lateral force are opposite to the upper rotor.

2.1.2 Pusher Propeller Aerodynamic Model

Pusher propeller serves as the main power for CHH during high-speed flight, generating forward thrust to counteract fuselage and rotor drag. As the pusher propeller operates in axial flow most of the time, the momentum theory of uniform inflow is applied to calculate the induced velocity of the pusher propeller to ameliorate the high calculation accuracy.

From momentum theory, the relationship between the average induced velocity v_{p} and the thrust T_{p} of the pusher propeller in forward flight satisfies the following Eq. (7).

$$T_{\mathrm{p}} = 2\pi\rho R^2 v_{\mathrm{p}}\sqrt{(\mu_{\mathrm{p}}\Omega_{\mathrm{p}}R_{\mathrm{p}})^2 + (\lambda_{\mathrm{p}}\Omega_{\mathrm{p}}R_{\mathrm{p}})^2}, \tag{7}$$

where ρ indicates air density, μ_p, Ω_p, R_p, λ_p denote the advance ratio, rotational speed, radius, and inflow ratio of the pusher propeller.

At the same time, the thrust and counter-torque of the pusher propeller are calculated from the blade element theory, as depicted in Eq. (8).

$$\begin{cases} T_p' = \frac{1}{2}\rho\pi R_p^2(\Omega_p R_p)^2 C_{tp} \\ M_{kP} = -\frac{1}{2}\rho\pi R_p^3(\Omega_p R_p)^2 C_{Mtp} \end{cases}, \tag{8}$$

where C_{tp} is the coefficient of pusher propeller thrust, and C_{Mtp} is the coefficient of pusher propeller counter-torque.

Combined with momentum theory and blade element theory.

$$T_p = T_p'. \tag{9}$$

Finally, the thrust and counter-torque under the horizontal propeller axis system are converted to the body axis system to obtain the forces and moments in the body axis system.

$$\begin{bmatrix} F_{xp} \\ F_{yp} \\ F_{zp} \end{bmatrix} = \begin{bmatrix} 0 \\ T_p \\ 0 \end{bmatrix}$$
$$\begin{bmatrix} M_{xp} \\ M_{yp} \\ M_{zp} \end{bmatrix} = \begin{bmatrix} 0 \\ -M_{kp} \\ 0 \end{bmatrix} + \begin{bmatrix} F_{zp}y_p - F_{yp}z_p \\ F_{xp}z_p - F_{zp}x_p \\ F_{yp}x_p - F_{xp}y_p \end{bmatrix}. \tag{10}$$

2.1.3 Fuselage Aerodynamic Model

During high-speed flight, fuselage parasite drag o also affects the flight performance of high-speed helicopters [19]. The corresponding aerodynamic drag, lift, and pitch moment of the fuselage without yaw are listed in Eq. (11).

$$\begin{aligned} L_F &= q_F \cdot C_L \cdot A_F \\ D_F &= q_F \cdot C_D \cdot A_F \\ M_F &= q_F \cdot C_M \cdot l_F \cdot A_F \end{aligned}, \tag{11}$$

where, q_F is the dynamic pressure of the fuselage, L_F is the characteristic length of the fuselage, and A_F is the characteristic area of the fuselage. C_D, C_L, and C_M are the drag coefficient, lift coefficient, and pitch moment coefficient of the fuselage, respectively.

Decompose the aerodynamic drag, lift, and pitch moment of the fuselage into the body axis system, and obtain the aerodynamic forces and moments of the fuselage in the body axis system as shown in Eqs. (12)–(13).

$$\begin{bmatrix} F_{XF} \\ F_{YF} \\ F_{ZF} \end{bmatrix} = \begin{bmatrix} \cos\alpha_F & 0 & -\sin\alpha_F \\ 0 & 1 & 0 \\ \sin\alpha_F & 0 & \cos\alpha_F \end{bmatrix} \times \begin{bmatrix} -D_F \\ 0 \\ -L_F \end{bmatrix}, \tag{12}$$

$$\begin{bmatrix} M_{XF} \\ M_{YF} \\ M_{ZF} \end{bmatrix} = \begin{bmatrix} 0 \\ M_F \\ 0 \end{bmatrix}, \tag{13}$$

where α_F is the angle of attack of the fuselage.

2.1.4 Horizontal Tail Aerodynamic Model

The upward drag of the horizontal tail is a function of the angle of attack, and the thrust and drag of the horizontal tail are depicted in Eq. (14).

$$\begin{bmatrix} L_h \\ D_h \end{bmatrix} = \begin{bmatrix} K_{qh}qA_h & 0 \\ 0 & K_{qh}qA_h \end{bmatrix} \begin{bmatrix} C_{lh} \\ C_{dh} \end{bmatrix} = \begin{bmatrix} K_{qh}qA_hC_{lh} \\ K_{qh}qA_hC_{dh} \end{bmatrix}, \tag{14}$$

where q is incoming flow pressure, A_h is the horizontal tail area, K_{qh} is the dynamic pressure loss coefficient of horizontal tail, C_{lh} is the lift coefficient of horizontal tail, C_{dh} is the drag coefficient of the horizontal tail.

Converting the horizontal tail aerodynamic forces and moments from the wind axis system to the body axis system.

$$\begin{bmatrix} F_{Xh} \\ F_{Yh} \\ F_{Zh} \end{bmatrix} = \begin{bmatrix} -\cos(\alpha_h - \varphi_h) & -\sin(\alpha_h - \varphi_h) & 0 \\ A - \sin(\alpha_h - \varphi_h) & -\cos(\alpha_h - \varphi_h) & 0 \\ 0 & 0 & 1 \end{bmatrix} \begin{bmatrix} D_h \\ L_h \\ 0 \end{bmatrix}, \tag{15}$$

$$\begin{bmatrix} M_{Xh} \\ M_{Yh} \\ M_{Zh} \end{bmatrix} = \begin{bmatrix} F_{Yh}z_h - F_{Zh}y_h \\ F_{Xh}z_h - F_{Zh}x_h \\ F_{Yh}x_h - F_{Xh}y_h \end{bmatrix}, \tag{16}$$

where α_h is the horizontal tail angle of attack and φ_h is the horizontal tail installation angle.

2.1.5 Vertical Tail Aerodynamic Model

The lift and drag generated by the vertical tail are directly related to the angle of attack of the vertical tail. According to the velocity and angle of attack at the vertical tail, the drag and lift at the vertical tail are shown in Eq. (17).

$$\begin{bmatrix} L_v \\ D_v \end{bmatrix} = \begin{bmatrix} K_{qv}qA_v & 0 \\ 0 & K_{qv}qA_v \end{bmatrix} \begin{bmatrix} C_{lv} \\ C_{dv} \end{bmatrix}, \tag{17}$$

where A_v is the vertical tail area, K_{qv} is the dynamic pressure loss coefficient of vertical tail, C_{lv} is the lift coefficient of vertical tail, and C_{dv} is the drag coefficient of the vertical tail.

Converting the forces and moments of the vertical tail aerodynamic forces to the body axis system.

$$\begin{bmatrix} F_{Xv} \\ F_{Yv} \\ F_{Zv} \end{bmatrix} = \begin{bmatrix} -\cos(\varphi_v - \alpha_v) & 0 & -\sin(\varphi_v - \alpha_v) \\ 0 & 1 & 0 \\ -\sin(\varphi_v - \alpha_v & 0 & \cos(\varphi_v - \alpha_v) \end{bmatrix} \begin{bmatrix} D_v \\ 0 \\ L_v \end{bmatrix}, \tag{18}$$

$$\begin{bmatrix} M_{Xv} \\ M_{Yv} \\ M_{Zv} \end{bmatrix} = \begin{bmatrix} F_{Zv} y_v - F_{Yv} z_v \\ F_{Xv} z_v - F_{Zv} x_v \\ F_{Yv} x_v - F_{Xv} y_v \end{bmatrix}, \tag{19}$$

where α_v is the vertical tail angle of attack and φ_v is the vertical tail installation angle.

Subsequently, the statistical and empirical techniques are utilized to calculate the aerodynamic forces and moments acting on the coaxial rotor, the pusher propeller, the fuselage, the horizontal tail, and the vertical tail.

$$\begin{cases} \sum F_X = F_{Xu} + F_{Xl} + F_{Xb} + F_{Xp} \\ \qquad + F_{Xh} + F_{Xv} - mg\sin\theta \\ \sum F_Y = F_{Yu} + F_{Yl} + F_{Yb} + F_{Yp} \\ \qquad + F_{Xh} + F_{Xv} - mg\cos\theta\cos\phi \\ \sum F_Z = F_{Zu} + F_{Zl} + F_{Zb} + F_{Zp} \\ \qquad + F_{Xh} + F_{Xv} + mg\cos\theta\sin\phi \\ \sum M_X = M_{Xu} + M_{Xl} + M_{Xb} + M_{Xp} + M_{Xh} + M_{Xv} \\ \sum M_Y = M_{Yu} + M_{Yl} + M_{Yb} + M_{Yp} + M_{Yh} + M_{Yv} \\ \sum M_Z = M_{Zu} + M_{Zl} + M_{Zb} + M_{Zp} + M_{Zh} + M_{Zv} \end{cases} \tag{20}$$

The subscripts of force and moment in Eq. (20) represent the aerodynamic forces and moments of upper rotor, lower rotor, fuselage, pusher propeller, horizontal tail, and vertical tail, m represents the helicopter mass, and g denotes the gravity acceleration.θ and φ are the pitch and roll angles, respectively. Finally, the nonlinear flight mechanics model of the whole aircraft is established. During stable flight, the resultant forces and moments acting on CCH are zero, and the triaxial angular rate and angular acceleration rate under body axis system are zero, which can be solved by the newton method.

To verify the confidence of the simplified model of CCH, X2 helicopter is selected as the sample helicopter to calculate its demanded power under a consistent flight state, and the model calculation results are compared with the test results in the literature [20], as shown in Fig. 4.

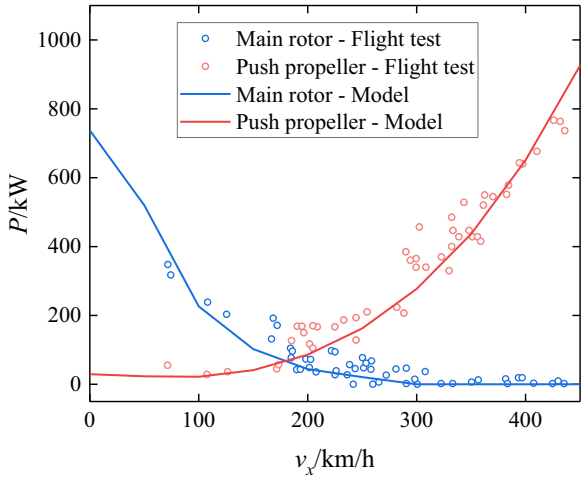

Fig. 4 Comparisons of coaxial compound high-speed helicopter model in power calculation

2.2 Variable-Speed Turboshaft Engine Model

Upon establishing the simplified model of coaxial high-speed helicopter, it is imperative to develop a suitable mathematical model of the variable-speed turboshaft engine to account for the effect of coaxial rotor speed variation on engine performance. A component-level model of variable-speed turboshaft engine is constructed by the Newton–Raphson (NR) method. A series of equations reflecting the co-operating relationships among components are formulated based on their aerothermodynamic relationships and rotating component characteristic data.

Specifically, it includes gas turbine inlet flow WG_4 continuity, power turbine inlet flow WG_{45} continuity, nozzle outlet pressure P_8 balance, gas turbine power HPT and compressor power HPC balance, and power turbine power HPP and external load power HPA balance [21]. The steady-state co-operating equations of the turboshaft engine component level model are shown in Eq. (21).

$$\begin{cases} E(1) = \dfrac{\mathrm{WG_4} - \mathrm{WG_{4c}}}{\mathrm{WG_{4c}}} \\ E(2) = \dfrac{\mathrm{WG_{45}} - \mathrm{WG_{45c}}}{\mathrm{WG_{45c}}} \\ E(3) = \dfrac{p_8 - p_{amb}}{p_{amb}} \\ E(4) = \dfrac{\mathrm{HPC}/\eta_g - \mathrm{HPT}}{\mathrm{HPT}} \\ E(5) = \dfrac{\mathrm{HPA}/\eta_p - \mathrm{HPP}}{\mathrm{HPP}} \end{cases}, \tag{21}$$

whereη_{gt} and η_{pt} are the rotor shaft mechanical transmission efficiencies of the gas turbine and power turbine, respectively. P_{amb} represents the atmospheric pressure at the outlet of the nozzle. WG_{4c} and WG_{45c} represent the calculated flow of the gas turbine and the power turbine, respectively.

When the turboshaft engine is in dynamic operation, the mass flow and pressure balance equations are consistent with steady-state operation, but the power at both ends of the compressor-gas turbine shaft and the power turbine shaft is no longer balanced, and the deviation power is applied for the acceleration and deceleration of the rotors. Therefore, the original two power balance equations are replaced by the rotor dynamics equations, as shown in Eq. (22).

$$\begin{cases} \dfrac{dN_g}{dt} = \dfrac{HPT - HPC/\eta_g}{N_g J_g}\left(\dfrac{30}{\pi}\right)^2 \\ \dfrac{dN_p}{dt} = \dfrac{HPP - HPA/\eta_P}{N_p J_p}\left(\dfrac{30}{\pi}\right)^2 \end{cases}, \tag{22}$$

where J_g and J_p are the moments of inertia for gas turbine and power turbine, respectively.

By optimizing and adjusting the power turbine efficiency at low speed, it becomes feasible to change the coaxial rotor speed by varying the power turbine speed. Furthermore, in combination with the multi-point model correction method, the component correction coefficients are multi-point matched to meet the accuracy requirements of the variable speed turboshaft engine model.

Subsequently, considering the characteristics of power transfer and the unified matching of power, forces coordinate system and time simulation scale, the simplified model of coaxial high-speed helicopter and the variable-speed turboshaft engine model are matched to establish an integrated model simulation platform for digital simulation research of multiple flight modes, the flowchart is shown in Fig. 5.

As depicted in Fig. 5, the engine model takes the demanded power of the simplified coaxial high-speed helicopter model as input and adopts the general characteristic diagram of the components to determine the common working relationship of each component of the engine. The steady-state calculation process of the engine involves solving the numerical solutions of the five equilibrium equations based on the NR method, and iteratively calculating along the residual reduction direction so that the solutions of the five balance equations satisfy the residual requirements, thereby obtaining the steady-state output results of the engine model. The relative speed of the gas turbine, the fuel flow rate, the pressure ratio coefficient of the compressor, the pressure ratio coefficient of the gas turbine, and the pressure ratio coefficient of the power turbine are selected as the initial guesses for the iterative solution. When the engine state changes, only the mass flow balance and static pressure balance in Eq. (21) need to be satisfied, and then combined with the rotor dynamics Eq. (22) to calculate the rotor speed at the next moment, using a once-through algorithm to perform dynamic calculations to improve the real-time performance of the model. A one-time dynamic calculation algorithm is employed to improve the real-time performance of the model.

The high-speed helicopter calculates the aerodynamic forces and moments of each component according to the control inputs, obtains the kinematic equations, and ultimately obtains the output state variables and the demanded power of the high-speed helicopter based on the coordinate transformation matrix. Connected with the engine closed loop, an integrated model simulation platform is finally established.

3 Demanded Power Prediction Model

When the CCH operates in multiple working modes, especially during the transition mode process, the demanded power of CCH cannot be measured directly, which involves variable speed and variable power output, resulting in sharp changes in demanded power. Since there are several helicopter parameters associated with CCH, which affect and restrict each other. Therefore, selecting the relevant parameters that correlate with demanded power is crucial to establish the demanded power prediction model for CCH.

3.1 Optimal Selection Method of Model Input Characteristic Parameters

The precision of demanded power prediction models is contingent upon the judicious selection of input characteristic parameters. Excessive input characteristic parameters result in some parameters containing invalid and noisy information that interferes with the model, thereby reducing the operation efficiency and prediction accuracy of the model. Conversely, when the input characteristic parameters are deficient, the information provided for model is insufficient to fully guarantee the quality of model. Due to the strong autocorrelation between some parameters of CCH, the model contribution of the autocorrelated parameters is lower than the actual value during the optimal selection and analysis. Accordingly, selecting appropriate parameters as input variables of the model through optimal selection is critical for developing the demanded power prediction model.

Random forest [22–24] (RF) is a machine learning algorithm with multi-class classification function. In view of the strong generalization ability of the RF in small samples, this paper proposes an optimal selection method for input variables of CCH demanded power prediction model based on the RF. By removing autocorrelated input characteristic parameters and evaluating the contribution of remaining input variables to the overall model, the optimal selection

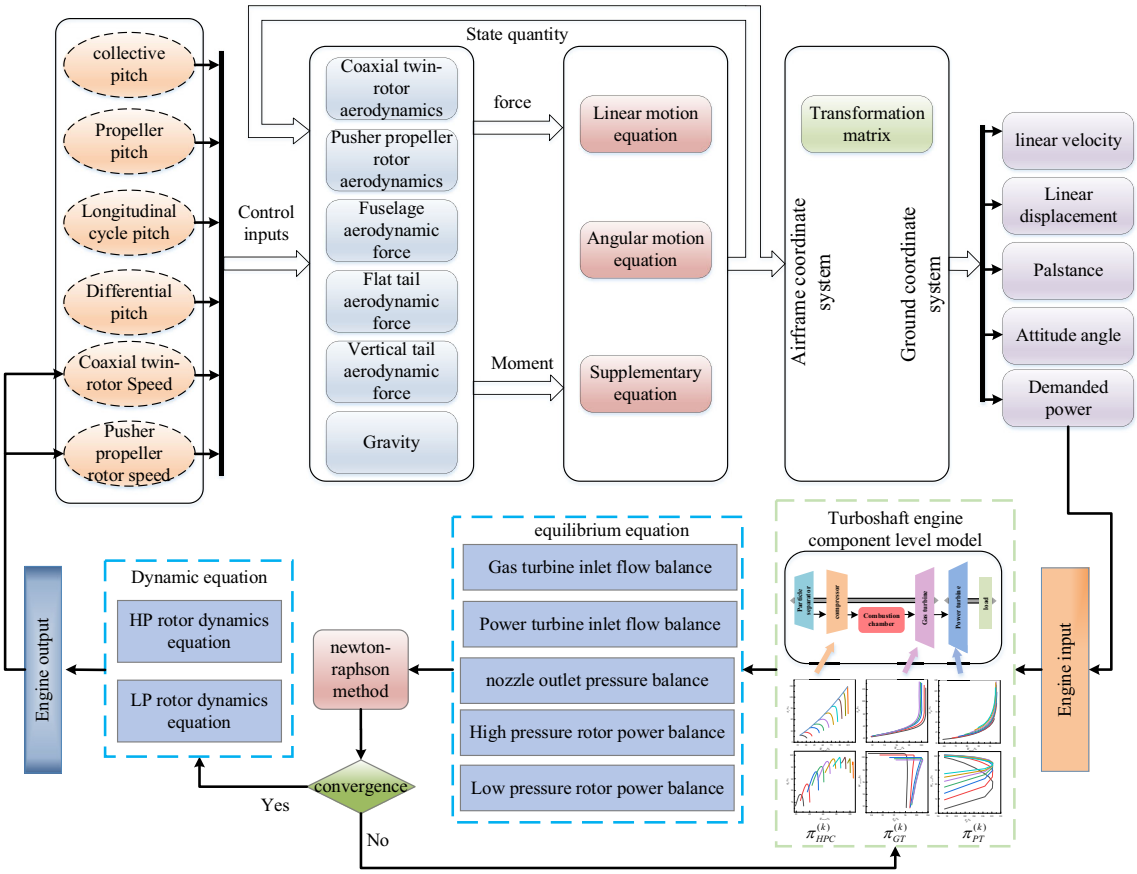

Fig. 5 Flowchart of integrated model simulation platform

method facilitates the identification of optimal input variables.

The RF method based on statistical learning theory is employed to select the relevant measurable parameters of CCH according to the process depicted in Fig. 6. Initially, based on the integrated simulation platform of high-speed helicopter/engine, a full-flight envelope data set is established by performing a full flight mission segment simulation to obtain a total of 100,000 original data sets for optimization, which includes most of the maneuvering processes in low-speed mode, low-speed mode, and transition mode, such as climbing, descending, accelerating, and decelerating maneuvers. Subsequently, the bootstrap sampling method is employed to obtain$n$ sub-training sets from the original training set, using with put-back sampling.

Each of the n sub-training sets adopts the classification and regression tree (CART) as the primitive learner. One sub-training set generates one decision tree, with no association between each tree. At each node of the tree, m ($m < M$) characteristic parameters are randomly selected from M characteristic parameters of the sample, taken $m = \text{int}(\sqrt{M})$. Each decision tree is allowed to grow completely without pruning until it can accurately classify the training sets or until all classification attributes are exhausted, resulting in a combinatorial learning model. In the process of building primitive learner based on CART, Gini coefficient is applied for feature selection of each node. The smaller the Gini coefficient, the higher the purity, the smaller the uncertainty and the more thorough the data segmentation. Knowing that there are m feature parameters and the probability of a sample belonging to class k is p_k, the Gini coefficient of probability distribution is defined as Eq. (23).

$$\text{Gini}(p) = \sum_{k=1}^{m} p_k(1 - p_k) = 1 - \sum_{k=1}^{m} p_k^2. \tag{23}$$

According to the definition of Gini coefficient, the Gini coefficient of sample set D is obtained, where C_k denotes the subset of samples belonging to the K-th category in sample set D. Then the Gini coefficient of sample set D is depicted in Eq. (24).

$$\text{Gini}(D) = 1 - \sum_{k=1}^{K} \left(\frac{|C_k|}{|D|} \right)^2. \tag{24}$$

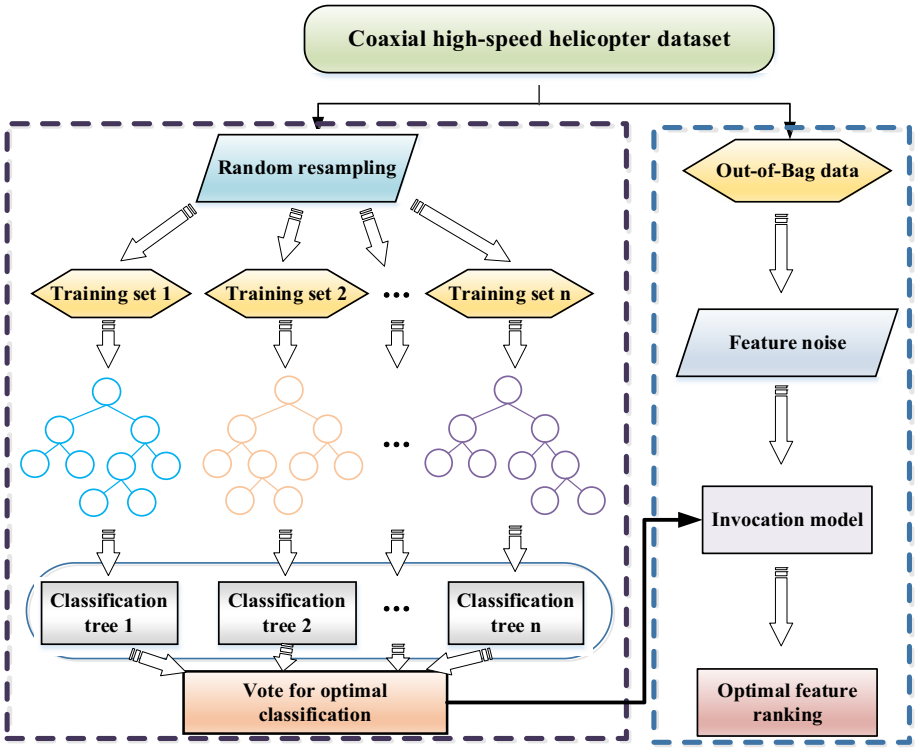

Fig. 6 Flowchart of optimal selection based on RF

If data set D is divided on a certain attribute value a according to feature$A$, D^1 and D^2 are obtained, then the Gini coefficient of set D under feature$A$ is shown below.

$$\mathrm{Gini}(D|A) = \sum_{v=1}^{2} \frac{|D^v|}{|N|} \mathrm{Gini}(D^v), \tag{25}$$

where Gini(D) denotes the uncertainty of set D, and Gini($D|A$) represents the uncertainty of set D after $A = a$ segmentation.

For each sample in the test sample set to be classified, n classification results are generated according to n decision tree models. The classification results of each decision tree are aggregated based on the voting principle to determine the optimal classification. The function of the classification decision model is as follows.

$$\mathrm{Cp} = \arg\max \left[\frac{1}{n} \sum_{I=1}^{n} I\left(\frac{n_{\mathrm{hi},c}}{n_{\mathrm{hi}}} \right) \right], \tag{26}$$

where, n is the number of decision trees in the RF, $I\left(\frac{n_{\mathrm{hi},c}}{n_{\mathrm{hi}}}\right)$ is the indicative function, $n_{\mathrm{hi},c}$ is the classification result of tree h_{i} on characteristic parameter$c$, and n_{hi} is the number of leaf nodes of the tree.

When extracting a subset of samples, the probability that each sample in the original data set is not extracted is given by $\left(1 - 1/N\right)^N$ (where, N is the total number of samples in original data set), which converges to 1/e $\approx$ 0.368 as N is large enough. Consequently, approximately 37% of the data set samples remain unselected, and those data set samples are referred to as out-of-bag (OOB) data. The OOB data are adopted to add noise to the input characteristic parameters to avoid over-fitting due to over-reliance on the test sample set. The reduction in OOB accuracy can be determined as its relevance to the target output, and its feature importance index is calculated as follows.

$$S_i = \frac{1}{N_{\mathrm{OOB}}} \sum_{N_{\mathrm{OOB}}}^{j=1} (A_j^0 - A_j^i), \tag{27}$$

where, N_{OOB} is the number of OOB samples, A_j^0 is the classification accuracy of OOB data before decision tree perturbation, and A_j^i denotes the classification accuracy of OOB data after decision tree perturbation.

Firstly, the 16 input control variables associated with helicopters and engines are normalized to eliminate the effect of inconsistent input parameter ranges on the evaluation function. Utilizing a random forest to rank the importance of these 16 parameters, including helicopter control parameters, the importance indicators of each parameter are obtained. The results are illustrated in Fig. 6. By setting a threshold for the importance index, the input variables with relatively high importance indices are selected, which represent the parameters most pertinent to the demanded power of the helicopter. To better emulate the real state of the helicopter, Gaussian

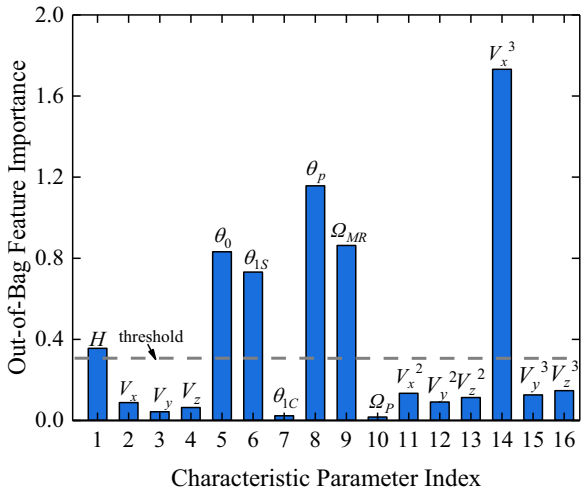

Fig. 7 Ranking of the characteristic parameter importance index based on RF

white noise is introduced into the relevant control parameters of the helicopter to simulate the real sensor noise.

According to the ranking of the importance index for characteristic parameter, the contribution capability of the characteristic parameters related to the demanded power model is screened and the redundant parameters are eliminated. Finally, the classification results of these parameters are presented in descending order of importance as follows: cubic forward flight speed, pusher propeller pitch, coaxial main rotor speed, collective pitch, longitudinal cycle pitch and altitude. The importance score is shown in Fig. 6, which is adopted to determine the optimal input combination of the demanded power prediction model (Fig. 7).

3.2 Establishment of Demanded Power Prediction Model

Considering the nonlinear characteristics of the engine operating process, this paper establishes a CCH demanded power prediction model based on the sample data. The model is trained offline using the mini-batch gradient descent (MBGD) neural network to obtain an accurate mapping that describes the input–output relationship. The structure of MBGD neural network is shown in Fig. 8. As such, the model exhibits robust fitting and generalization capabilities and effectively addresses sample noise learning problems, resulting in excellent nonlinear approximation performance.

The output expression for the m-th ($m \geq 2$) layer, and the i-th node in the forward propagation process of MBGD neural network is illustrated in Eq. (28).

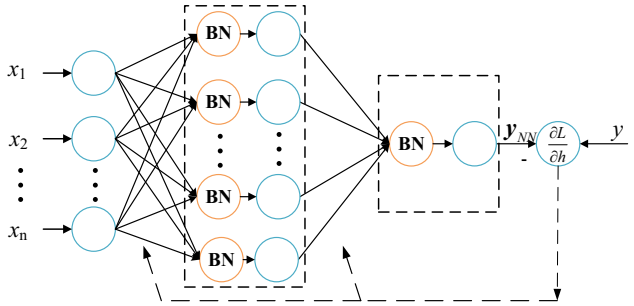

Fig. 8 Structure of MBGD neural network for demanded power prediction model

$$a_i^m = \sum_{j=1}^{n_{m-1}} W_{ij}^m h_j^{m-1} + b_i^m$$
$$h_i^m = f(a_i^m), \tag{28}$$

where, n_{m-1} is the number of nodes in $m-1$ layer, W_{ij}^m represents the weight of the i-th neuron in m-th layer, b_i^m is the bias in m-th layer, h_j^{m-1} and h_i^m are the output of the$j$-th node in$m$-1 layer and the i-th node in$m$-th layer, respectively. $f(\cdot)$ is the activation function.

After completing the forward propagation process, if the output layer is still unable to match the desired output, it is transferred to the backward propagation process, and search the weight vector dynamically according to the error function to minimize the loss function. The mini-batch gradient descent (MBGD) method for training neural networks is proposed, which combines the advantages of the batch gradient descent (BGD) and stochastic gradient descent (SGD) methods. The sample is divided into several subsets called mini-batches, and the algorithm calculates the loss function using only one mini-batch in each iteration. Consequently, the MBGD method is faster than the BGD method and has higher accuracy than the SGD method. The expression of the loss function is depicted in Eq. (29).

$$L(e) = \min_{W,b} \sum_{i=1}^{N_W} \frac{1}{2} \left\| \boldsymbol{y}_{NN}(x_i) - \boldsymbol{y}_i \right\|^2, \tag{29}$$

where N_W is the sample capacity and $y_{NN}(x_i)$ is the output of the neural network.

The weight and bias gradient calculation of the m-th layer neural network and the weight reverse update after each iteration are exhibited in Eq. (30).

$$\begin{aligned} \nabla W_{ij}^m &= \frac{\partial L(e)}{\partial W_{ij}^m} = h_j^m \otimes \delta_j^{m+1} \\ \nabla b_i^m &= \frac{\partial L(e)}{\partial b_j^m} = \delta_j^{m+1} \\ W_{ij}^m &= W_{ij}^m - \eta \nabla W_{ij}^m \\ b_i^m &= b_i^m - \eta \nabla b_i^m, \end{aligned} \tag{30}$$

where δ_j^{m+1} represents the derivative of the$j$-th node of $m+1$ layer, η is the learning rate.

Utilizing the aforementioned principles, the helicopter demanded power prediction model is established by offline training using the MBGD neural network. The model takes the cubic forward flight speed, pusher propeller pitch, coaxial main rotor speed, collective pitch, longitudinal cycle pitch, and altitude as inputs. It takes the demanded power of CCH in the current state as output, all the inputs can be measured by sensors, making the model feasible.

The expression of the MBGD neural network mapping is then constructed as follows.

$$\begin{aligned} &\mathbf{Y} = f_{NN}(\mathbf{x}) \\ &\mathbf{x} = [V_x^3,\ \theta_p,\ \boldsymbol{\Omega}_{MR},\ \theta_0,\ \theta_{1S},\ H]. \end{aligned} \tag{31}$$

To ensure that the established helicopter demanded power model can meet the requirements of accuracy and real-time performance, a three-layer MBGD neural network structure is adopted. In addition to the input and output layer nodes defined in the above formula, 15 hidden layer nodes are set, and the implicit layer and output layer activation functions are set as tansig and purelin functions, respectively. The collected data are completely stimulated by the integrated simulation platform of high-speed helicopter/engine and normalized to serve as the training and testing samples of the neural network.

The precision of the prediction model is verified by test sample data. Figure 9 shows the relative error percentage between the output of the demanded power prediction model and the sample output. The relative errors of the output parameter are less than 1.4%. With the exception of a few points, the majority of the sample errors are within 0.6%. Therefore, the overall high precision of the model allows for the prediction of demanded power ahead of time.

With the variable rotor speed of the CCH, the coaxial main rotor speed is not constant. Furthermore, due to the pusher propeller generates the primary thrust during high-speed flight, the conventional collective pitch feedforward method is bound to be ineffective in ameliorating the overshoot and sag of the power turbine speed. In the literature

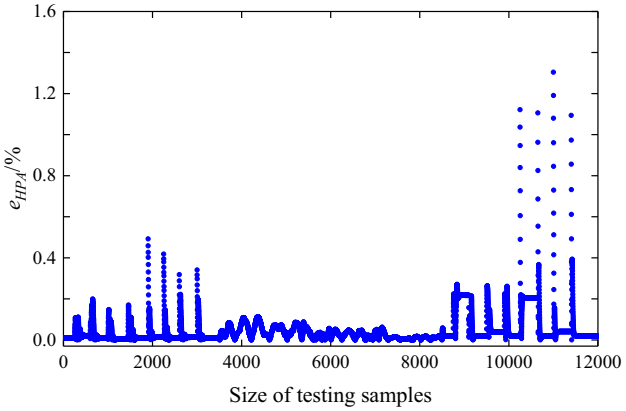

Fig. 9 Relative error between the output of the neural network and the sample output

[15], a torque error feedforward method is proposed for variable rotor speed helicopter, as demonstrated in Eq. (32). It obtains the engine demanded torque according to the coaxial main rotor speed and the power turbine speed, and the error with the real torque is adopted as the feedforward. Nevertheless, the torque error feedforward is only applied to the gas turbine acceleration loop, which still has a certain lag in the compensation effect. Furthermore, the torque error feedforward method is only applicable on the ground and cannot be applied to the large envelope.

$$\Delta = T_{\mathrm{qe,p}} \cdot \frac{\Omega_{\mathrm{MR}}}{N_{\mathrm{p}}} - T_{\mathrm{qe}}. \tag{32}$$

Consequently, this paper proposes an integrated control method based on the double feedforward of demanded power prediction as shown in Eq. (33). Based on the demanded power prediction model, the error between the demanded power prediction model and the real demanded power is applied as the feedforward. The feedforward is corrected by an adaptive compensation coefficient to achieve adaptive compensation for turboshaft engine control system.

$$\begin{aligned} &\mathrm{HPA}_p = f_{NN}(V_x^3,\ \theta_{\mathrm{p}},\ \boldsymbol{\Omega}_{\mathrm{MR}},\ \theta_0,\ \theta_{1S},\ V_x) \\ &\Delta = K(\mathrm{HPA_p} - \mathrm{HPA_r}) \\ &K = f(H,\ V_x), \end{aligned} \tag{33}$$

where K represents feedforward gain. To be suitable for the full envelope, the gain self-adjustment is achieved by combining similar transformation and interpolation search.

4 Design of High-Order Filter for Gas Turbine Acceleration

The structure of the integrated control of coaxial high-speed helicopter/engine based on power prediction feedforward is

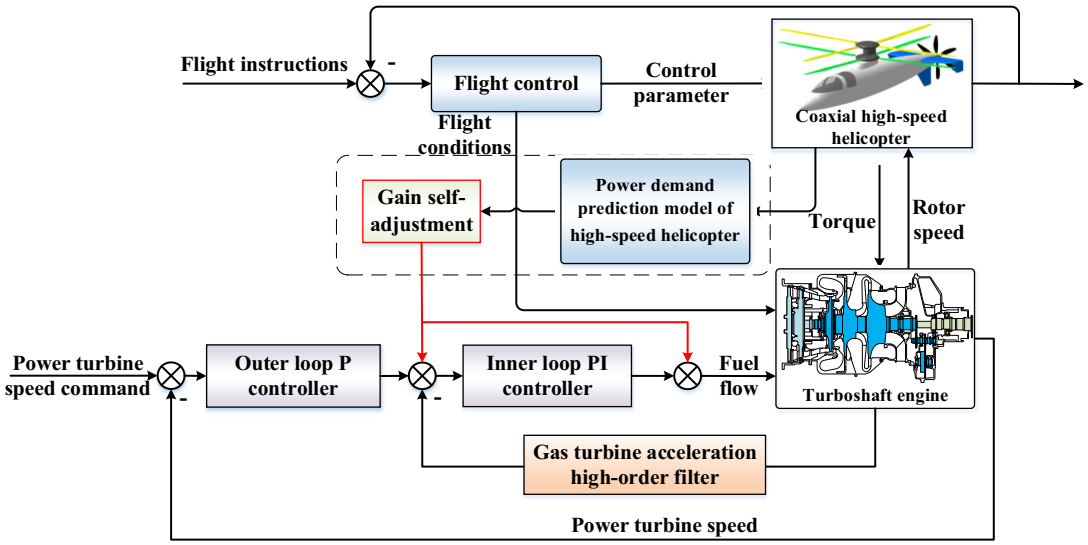

Fig. 10 Integrated control structure of coaxial high-speed helicopter/engine based on power prediction feedforward

shown in Fig. 10. Based on measurable engine parameters, the high-order filter is applied to predict real-time changes in gas turbine speed, thereby estimating the gas turbine acceleration. Based on the integrated simulation platform of high-speed helicopter/engine, the characteristic parameters obtained from the RF are transferred to the demanded power prediction model. The model output is compared with the real power calculated by engine torque and power turbine speed to obtain compensation. Subsequently, the compensation is transmitted to both the acceleration loop of the gas turbine and the fuel flow position for feedforward through gain self-adjustment. Finally, the double feedforward is superimposed to compensate the final output fuel control quantity and realize the integrated control of coaxial high-speed helicopter/engine.

To realize cascade PID control of turboshaft engines based on Ngdot, a gas turbine acceleration estimation method needs to be designed to estimate the real-time change rate of gas turbine speed based on engine measurable parameters. In the engine system, due to system noise and other factors, the gas turbine rotor acceleration calculated by differential equations as an estimated value suffers from jumps, and there is a sudden change in fuel flow under certain large load changes.

The acceleration of a conventional gas turbine is calculated by Eq. (34), where ΔT is the sampling time, and k represents the current moment.

$$a_{\mathrm{g}}(k) = \frac{N_{\mathrm{g}}(k) - N_{\mathrm{g}}(k-1)}{\Delta T}. \tag{34}$$

To overcome the shortcomings of the first-order difference or center difference methods, a higher-order filter for gas turbine acceleration estimation method is designed. As illustrated in Eq. (35), the higher-order filter filters out the high frequency noise of the velocity signal, the filter has a simple structure, high real-time performance, and linear phase.

$$G_{\mathrm{h}} = \sum_{n=0}^{N-1} h_n z^{-n}. \tag{35}$$

For this higher-order filter, the amplitude-frequency characteristics can be written as:

$$\begin{aligned} H(e^{jw}) &= \left[\sum_{n=1}^{N/2} b(n)\cos\left(\left(n-\frac{1}{2}\right)\omega\right)\right] e^{jw\left(\frac{N-1}{2}\right)} \\ b(n) &= 2h\left(\frac{N}{2}-n\right),\ n = 1, 2, \ldots, \frac{N}{2}. \end{aligned} \tag{36}$$

The corresponding phase function is $\theta(\omega) = -\frac{N-1}{2}\omega$, and the group delay is $\tau(\omega) = -\frac{N-1}{2}$. Assuming a speed sampling frequency of 0–5000Hz and a sampling period of 25ms for a closed-loop control system, N should satisfy:

$$t = \frac{N-1}{0.5k} < 25\ \mathrm{ms}, \tag{37}$$

where, t is the sampling frequency. From the above formula, it can be inferred that the order of the filter should satisfy $N \leq 12$. Therefore, let $N = 12$ to obtain the discrete transfer function form of the designed high-order filter as follows:

$$\begin{aligned} G_{\mathrm{h}} = h_0 + h_1 z^{-1} + h_2 z^{-2} + h_3 z^{-3} + h_4 z^{-4} + h_5 z^{-5} + h_6 z^{-6} - \cdots \\ \left(h_5 z^{-7} + h_4 z^{-8} + h_3 z^{-9} + h_2 z^{-10} + h_1 z^{-11} + h_0 z^{-12}\right). \end{aligned} \tag{38}$$

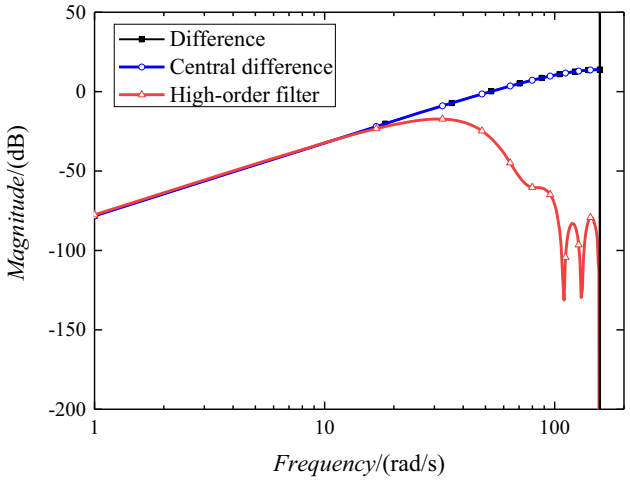

Fig. 11 Amplitude frequency characteristics of high-order filters

From the above equation, it can be seen that the expression has a coefficient duality feature, where $h_0 = -0.0099$, $h_1 = 0.0061$, $h_2 = 0.0267$, $h_3 = 0.0597$, $h_4 = 0.0912$, $h_5 = 0.0786$, $h_6 = 0.0001$.

In the typical fuel control bandwidth frequency range of 0–19 rad/s, the high-order filter maintains the characteristics of the original first-order difference, while designing an obvious frequency cutoff in the high-frequency range. The high-order filter further suppresses high-frequency interference without losing fuel control characteristics, and also make it possible to realize cascade PID control of rotational acceleration, which is conducive to increasing the bandwidth of the closed-loop system response. The amplitude frequency characteristics of the high-order filters are depicted in Fig. 11.

As illustrated in Fig. 11, within 3 Hz, the characteristics of the high-order filter are consistent with the first-order and center difference methods, indicating that in this frequency range, the estimation effect of the high-order filter for gas turbine acceleration is consistent with the center difference method. However, when the frequency is higher than 8 Hz, the high-order filter exhibits a cutoff characteristic, which is beneficial for attenuating high-frequency noise and alleviating the large range of abrupt changes in the estimated value of the rotational acceleration within a single sampling step.

5 Simulation Verification

To evaluate the effectiveness of the integrated control based on power prediction feedforward in different modes of the CCH, the CCH accelerates from 0 km/h in 40 s and to 450 km/h in 160 s at the flight altitude of 3000 m. Maneuvers are performed in low-speed mode, transition mode and high-speed mode, respectively. The results are compared with the conventional control without feedforward and the torque error feedforward control method. The comparison results are illustrated below.

As shown in Fig. 12, in the low-speed flight mode, the demanded power of coaxial main rotor increases with flight speed. However, due to a certain response delay in the turboshaft engine, the power turbine speed drops instantaneously, while the power consumed by the coaxial main rotor still dominates. Figure 12a–f demonstrate that the integrated control method based on double feedforward of the demanded power prediction can effectively suppress the relative speed overshoot and sag of the power turbine. Compared with the torque error feedforward, the maximum sag is decreased by 28.1% and the maximum overshoot is decreased by 25.6%. Moreover, during the maneuvering process of CCH, the coaxial main rotor demanded power changes rapidly. The power prediction feedforward control is more responsive and exhibits better dynamic control quality. On account of the engine output torque measurement lags behind, the large inertia of rotor, and the aerodynamic connection between gas turbine and power turbine. The torque error feedforward is adopted to correct the Ngdot command cannot compensate the fuel flow in time. However, the demanded power feedforward employs several cross-linking parameters from coaxial high-speed helicopter/engine into the predicted model. By adopting the error between prediction power and real demanded power as the feedforward to correct the Ngdot command and fuel flow command online, enabling more rapid compensation by performing feedforward compensation in both control loops at the same time.

In transition mode, as depicted in Fig. 13, the power turbine speed is continuously reduced as the airspeed increases to avoid blade tip stall. To maintain the constant lift and thrust, the pusher propeller pitch is increased while the collective pitch is decreased. The proportion of coaxial main rotor power gradually decreases, the proportion of the power of the pusher propeller gradually increases. These changes are coordinated and result in an increase in total demanded power of CCH. As shown in Fig. 13 (e), during the accelerated climb maneuver starting at 134s, coaxial main rotor speed continues to decrease and turboshaft engine response lags behind causing an instantaneous sag in power turbine speed. Since the variation of the torque error no longer accurately reflects the demanded power of CCH, which cannot meet the dynamic control requirements. Compared with the torque error feedforward control method, the integrated control method based on double feedforward of demanded power prediction decreases the sag of power turbine speed by 25.3%. The fuel variation curve shown in Fig. 13c indicates that the fuel flow variation curve is smoother and the fuel flow variation trend is more moderate.

In high-speed mode, the coaxial main rotor is unloaded, and the pusher propeller provides the forward thrust. As the forward flight speed reaches 450 km/h, the demanded power

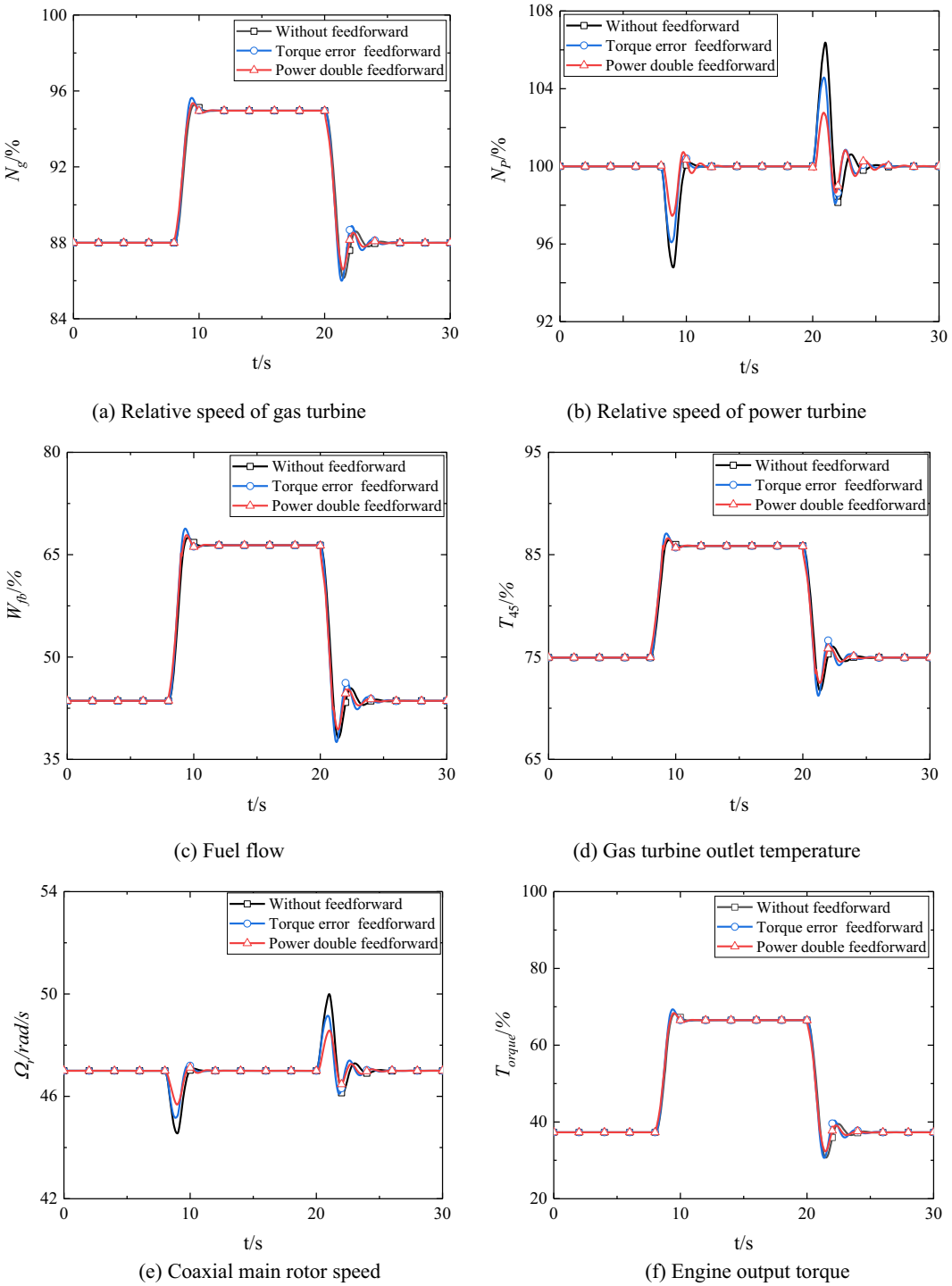

Fig. 12 Comparison of power prediction feedforward control effect in low-speed mode

of CCH is primarily composed of the power consumed by the pusher propeller. As shown in Fig. 14, the relative speed of the power turbine decreases to 80%. By adjusting the pusher propeller pitch, the CCH climbs after 190s and decelerates after 210s. The demanded power of the CCH changes sharply in this process, resulting in the corresponding change of the engine output torque. Due to the mechanical coupling and gas path coupling between the turboshaft engine and the CCH, the delayed response of the engine leads to overshoot and sag of the power turbine speed. The integrated control method based on double feedforward of demanded power prediction can respond to the turboshaft engine quickly compared to the

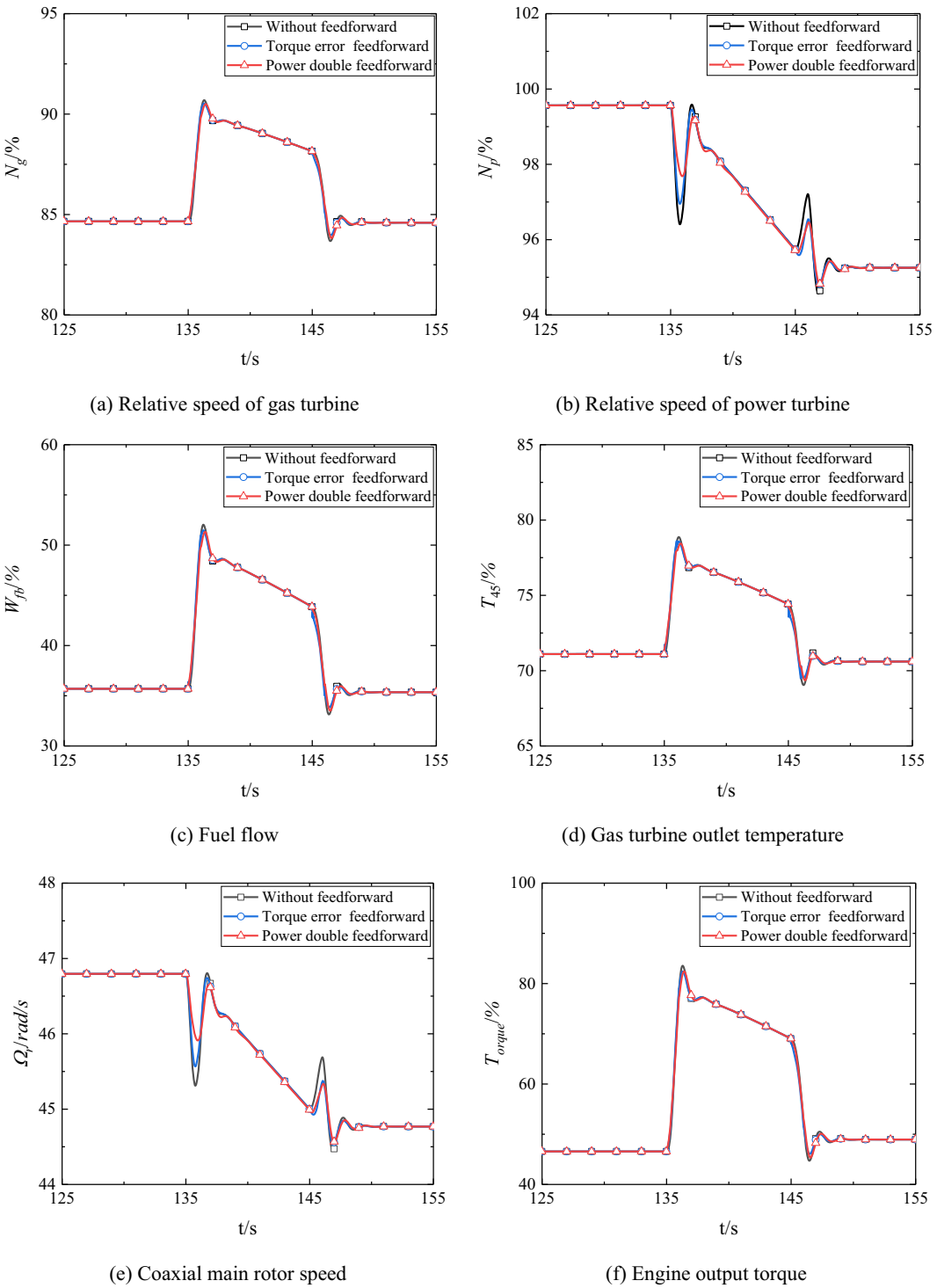

(a) Relative speed of gas turbine

(b) Relative speed of power turbine

(c) Fuel flow

(d) Gas turbine outlet temperature

(e) Coaxial main rotor speed

(f) Engine output torque

Fig. 13 Comparison of power prediction feedforward control effect in transition mode

torque error feedforward control method. The maximum sag of the power turbine relative speed is decreased by 30.1% and the maximum overshoot is decreased by 17.5%. As shown in Fig. 14a, d, the entire engine operation process remains stable and reliable. The integrated control method based on double feedforward of demanded power prediction has better stability, dynamic performance, and superior robustness.

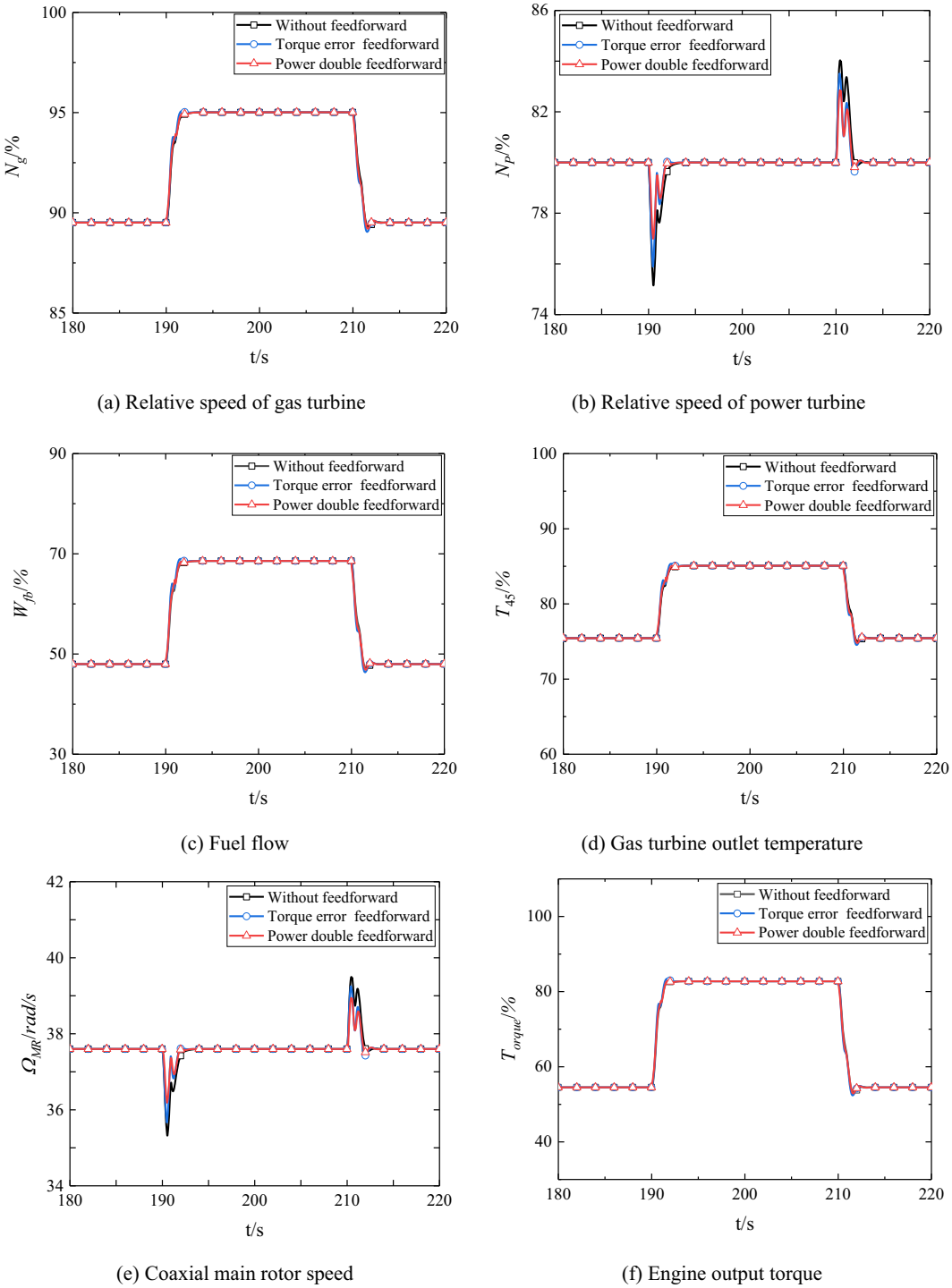

(a) Relative speed of gas turbine

(b) Relative speed of power turbine

(c) Fuel flow

(d) Gas turbine outlet temperature

(e) Coaxial main rotor speed

(f) Engine output torque

Fig. 14 Comparison of power prediction feedforward control effect in high-speed mode

6 Conclusion

The research on integrated control method of coaxial helicopter/engine based on power prediction feedforward has been conducted, and an integrated control method of coaxial high-speed helicopter/engine based on demanded power prediction double feedforward is proposed. The following conclusions can be drawn.

1. By analyzing the contribution capability of parameters related to the demanded power model and introducing noise to the input variables with OOB data to eliminate

redundant parameters. The six optimal input variables of cubic forward flight speed, pusher propeller pitch, coaxial main rotor speed, collective pitch, longitudinal cycle pitch, and altitude are finally obtained.

2. By employing the RF method to select relevant measurable parameters for CCH, an optimal selection of inputs for the prediction model is obtained. Subsequently, MBGD neural network is adopted to establish the demanded power prediction model of CCH. The relative error of the demanded power prediction model is less than 1.4%.
3. Under different flight conditions, the integrated control method of coaxial high-speed helicopter/engine based on demanded power prediction double feedforward decreases the overshoot and sag of power turbine speed by more than 17.5% and 25.3%, respectively, compared with the torque error feedforward control method. As a result, it helps to enhance the stability, dynamic performance, and robustness of the control system.

Funding This article was funded by National Natural Science Foundation of China (Grant no. 52202474), National Science and Technology Major Project (Grant no. J2019-I-0020-0019), Innovation Centre for Advanced Aviation Power (Grant no. HKCX2022-01-026-829 03), Fund of Prospective Layout of Scientific Research for NUAA (No.1002-ILA22037-1A2), State Key Laboratory of Mechanics and Control for Aerospace Structures (Grant no. MCAS-S-0323G01).

Data availability The data that support the findings of this study are available from the corresponding author, Haibo Zhang], upon reasonable request.

References

1. Rosen KM (2008) A prospective: the importance of pusher technology to the development of helicopter systems with a vision for the future the 27th Alexander A. Nikolsky lecture [J]. J Am Helicopt Soc 53(4):307–337
2. Chi C, Yan X, Chen R et al (2019) Analysis of low-speed height-velocity diagram of a variable-speed-rotor helicopter in one-engine-failure [J]. Aerosp Sci Technol 91:310
3. Blackwell R, Millott T (2008) Dynamics design characteristics of the sikorsky x2 technology demonstrator aircraft. In: Proceedings of the American Helicopter Society 64th Annual Forum, F, [C]
4. Ferguson K, Thomson D (2013) Flight dynamics investigation of compound helicopter configurations [J]. J Aircr 52(1):1–12
5. Kalinin D (2014) Multithreaded continuously variable transmission synthesis for next-generation helicopters. In: Proceedings of the Congress of the International Council of the Aeronautical Sciences, F, [C]
6. Yeo H, Johnson W (2009) Optimum design of a compound helicopter [J]. J Aircr 46(4):1210–1221
7. Snyder CA, Acree JRCW (2012) Preliminary assessment of variable speed power turbine technology on civil tiltrotor size and performance. In: Proceedings of the American Helicopter Society 68th Annual Forum, F, [C]
8. Berger T, Blanken CL, Lusardi JA et al (2022) Coaxial-compound helicopter flight control design and high-speed handling qualities assessment [J]. J Am Helicopt Soc 67(3):98
9. Cao Y, Wang M, Li G (2021) Flight dynamics modeling, trim, stability, and controllability of coaxial compound helicopters [J]. J Aerosp Eng 34(6):04021084
10. Ebert FJ, Driscoll JT, Graham JRB et al (1993) Helicopter engine control having lateral cyclic pitch anticipation [Z]. Google Patents
11. Smith B, Zagranski R. Closed loop bench testing of the next generation control system for helicopter engines. In: Proceedings of the AHS International, 58 th Annual Forum Proceedings-, F, 2002 [C]
12. Driscoll JT, Hull J, Mattice JS. Rotor torque predictor [Z]. US
13. Liguo S, Rixian W, Jianguo S, Haibo Z (2011) Subsystem disturbance rejection control of turbo-shaft engine/helicopter based on cascade ADRC [J]. J Beijing Univ Aeronaut Astronaut 37(10):1312–1316 (**in Chinese**)
14. Wang Y, Zheng Q, Zhang H et al (2020) Research on integrated control method for helicopter/turboshaft engine with variable rotor speed based on the error between engine required and real output torque [J]. Arab J Sci Eng 45(8):6529–6540
15. Chen L, Xin J (2022) Flight dynamic modeling and verification of coaxial high-speed helicopter [J]. Flight Dyn 40(2):25–32
16. Gao H, Shi H, Zou X et al (2022) Flight dynamics modeling and control of a new type high-speed helicopter in take-off and landing. In: Proceedings of the international conference on unmanned aircraft systems (ICUAS), Dubrovnik, CROATIA, F
17. Tischler MB (2022) Flight control technology advancements and challenges for future rotorcraft 40th Alexander A. Nikolsky Honorary Lecture [J]. J Am Helicopt Soc 67(4):1
18. Ou F (2016) Research on trimming, flight performance calculation method of coaxial helicopter [D]. Nanjing University of Aeronautics and Astronautics
19. De Gregorio F (2019) Helicopter fuselage model drag reduction by active flow control systems [J]. J Am Helicopt Soc 64(2):022001.1-022001.15
20. Walsh D, Aircraft S, Weiner S et al (2011) High airspeed Testing OF the Sikorsky X2 Technology (TM) demonstrator
21. Wenrong Y (2008) Research on integrated modeling, control and optimization of turboshaft engine/rotor. [D]. Nanjing University of Aeronautics and Astronautics
22. Biau G, Scornet E (2016) A random forest guided tour [J]. TEST 25(2):197–227
23. Belgiu M, Drăguţ L (2016) Random forest in remote sensing: a review of applications and future directions [J]. ISPRS J Photogramm Remote Sens 114:24–31
24. Smith A, Sterba-Boatwright B, Mott J (2010) Novel application of a statistical technique, Random Forests, in a bacterial source tracking study [J]. Water Res 44(14):4067–4076